

Microstructural Characterization and Electrochemical Behaviour of TiC-reinforced Mo-based Composites

Renheng Han¹, Qinyang Zeng¹, Yanqin Zhu¹, Ziming Bao¹, Ming Tang^{1,2},
Hexin Zhang^{1,2,*}, Chengzhi Zhao^{1,2,*}

¹ College of Materials Science and Chemical Engineering, Harbin Engineering University, Harbin 150001, China

² Key Laboratory of Superlight Materials and Surface Technology, Ministry of Education, Harbin, Engineering University, Harbin 150001, China

*E-mail: zhanghx@hrbeu.edu.cn

Received: 19 July 2020 / *Accepted:* 23 September 2020 / *Published:* 31 October 2020

This article reports on using the spark plasma sintering (SPS) process to prepare a TiC/Mo-based alloy. The engineering application performance of the alloy was evaluated using X-ray diffraction (XRD) and transmission electron microscope (TEM) characterization methods. The electrochemical corrosion behaviour of the TiC/Mo alloy was studied by potential polarization, and the microstructural characteristics of corrosion products were characterized and analysed using scanning electron microscopy (SEM) and energy dispersive spectrometry (EDS). The electrochemical behaviours of TiC/Mo alloys within a variety of different corrosive environments were examined, revealing the influence of corrosion resistance and the corrosion mechanism. The results showed that the TiC/Mo composite prepared by the SPS method had excellent engineering properties and met the needs of practical applications. With increasing pH, the electrochemical corrosion rate of the TiC/Mo alloy gradually increased, as did the corrosion tendency. The surface corrosion of the TiC/Mo alloy gradually strengthened, and an oxidation-reduction reaction occurred under the action of electric current. Oxides in the form of films and agglomerated structures were formed to cover the surface of the alloy matrix. Corrosion was caused by pitting at places where alloying elements were added as well as impurity-rich areas, irregular surfaces and narrow cracks. As the degree of corrosion intensified, the corrosion pits gradually changed from black or dark brown ring-shaped spots to a vortex-like uneven corrosion morphology. The confluence of corrosion vortices further intensified the corrosion of the alloy surface. TiC/Mo alloys have good practical engineering applications and corrosion resistance within low-concentration alkaline environments.

Keywords: TiC; Molybdenum alloy; electrochemical behaviour; polarization curves; AC impedance spectra

1. INTRODUCTION

With the continuous promotion of molybdenum and molybdenum alloy applications, higher requirements are being put forward for its comprehensive performance [1-3]. A molybdenum alloy with TiC as the reinforcing phase is widely utilized within the fields of machinery, chemical industries, electronics, metallurgy and aviation due to its excellent high-temperature strength, toughness and structural stability [4-7]. As a result of these practical applications for molybdenum alloys, the working environments are usually characterized by high temperatures and pressures and strong corrosive atmospheres [8]. Therefore, it is necessary to conduct in-depth research on the high-temperature oxidation resistance, high-temperature mechanical properties, and corrosion resistance of molybdenum alloys [9-10]. At present, there are few studies on the corrosion resistance of TiC-enhanced molybdenum alloys, making it necessary to conduct in-depth explorations within this field.

Previous studies [11-13] have concluded that in addition to the easy dissolution of molybdenum alloys in mixed acids such as aqua regia and HNO_3 +HF, molybdenum alloys have excellent corrosion resistance within various acidic media. However, molybdenum alloys have poor corrosion resistance in Cl^- salt solutions and alkaline environments [14]. Researchers such as J. Besson conducted experimental analyses on the polarization behaviour of molybdenum alloys in aqueous solutions and noted that oxide film passivation layers were formed on their surfaces, enabling the molybdenum alloys to show good corrosion resistance [15]. Further research found that the passivation film on the surface of a molybdenum alloy in an aqueous solution is mainly composed of Mo and MoO_2 [16-17]. However, there are also some researchers who disagree with the above viewpoints. They believe that the passivation of molybdenum alloy is essentially a chemical adsorption process and that the surface passivation film is a dense film composed of MoO_2 and $\text{MoO}(\text{OH})_2$ [18-20]. At present, related research on the corrosion of molybdenum alloys has mainly focused on the preparation methods and coating systems of corrosion-resistant coatings. However, research on the electrochemical corrosion behaviour of TiC-enhanced molybdenum alloys in alkaline solutions and the influence of the corrosion process are not sufficiently systematic. The overall performance of these alloys in a strong corrosion environment is significantly reduced to varying degrees.

Combining the research status of refractory metals and cemented carbides at home and abroad in corrosive environments, this paper uses the spark plasma sintering (SPS) method to prepare TiC-reinforced molybdenum-based alloys and tests the microstructure, polarization curve, AC impedance spectroscopy and corrosion morphology of the alloy. The effect of different concentrations of alkaline corrosion media on the corrosion of TiC-enhanced Mo-based alloys is also studied, and their corrosion mechanism is discussed in depth. This study provides the necessary theoretical support for the application of TiC-reinforced molybdenum-based alloys under different OH^- concentration usage conditions and provides a certain theoretical basis for research on improving the corrosion resistance of alloys.

2. EXPERIMENTAL METHOD

2.1. Materials

The SPS equipment used in this experiment is an LHPD250 apparatus designed and manufactured by FCT Systeme GmbH in Germany. The experimental materials used pure molybdenum powder and pure TiC powder, and 5% (w.t.) TiC was added to the pure molybdenum powder as the raw material for the TiC-reinforced Mo-based alloy (hereafter referred to as the TiC/Mo alloy). The ball mill process was used to mix the element powders. The ball mill parameters were as follows: the ball-to-material ratio was 2:1, the ball milling time was 5 h, the rotation speed was 200/rpm and the ball mill tank was filled with argon as a protective gas. The ball mill process was as follows: after dry mixing, the powder was compacted at the bottom of the ball mill tank, and then the ball was floated on it. Then, ethanol was added as the ball milling medium, and mixing was continued. The powder was then treated in a vacuum drying oven at 100°C for 1 hour and sieved through a 200 mesh sieve. Then, using an analytical balance, 300 grams of powder was measured and placed in a Ø40 graphite mould. Before charging, graphite paper was attached to the inside of the mould and became the contact surface between the head and the powder. Then, the mould was placed in the SPS furnace. The temperature rose from room temperature to 1700°C at a rate of 100 K/min. Additionally, the pressure rose from 5 MPa to 30 MPa. Then, the temperature was maintained for 9 minutes before finally being cooled in the furnace.

2.2. Electrochemical tests

An electrochemical test of the TiC/Mo alloy was carried out with a Zahner electrochemical corrosion workstation. The alloy samples were cut into 5×5×5 mm blocks, polished, dried and packaged for use. The corrosion reagent used was a KOH solution. The pH values of the corrosion reagents were 8, 9, 10, and 11. A three-electrode system was used to measure the polarization curve and AC impedance. The TiC/Mo alloy was used as the working electrode, a platinum electrode was used as the auxiliary electrode and a saturated calomel electrode was used as the reference electrode. The test temperature was room temperature (25°C). The potentiodynamic polarization curve parameters selected the initial potential relative to the open circuit potential to be lower than 750 mV, the termination potential to be 2.0 V and the scan rate to be 0.5 mV/s. The scanning frequency range of the electrochemical impedance spectroscopy (EIS) analysis test was selected from 100 kHz to 0.01 Hz, and the sine wave excitation signal amplitude was 5 mV. ZSimpWin software was used to analyse and fit the electrochemical impedance data and equivalent circuit.

2.3. Microstructure tests

The microstructural observations and composition analysis were conducted using scanning electron microscopy (SEM) and energy dispersive spectroscopy (EDS) (Quanta 200, FEI Company). A nonconductive oxide was deposited on the samples prior to analysis (3ΔL - TEC model SCD005). The voltage of the scanning electron microscope was 15 kV. To more accurately analyse the surface

morphology of the alloy, the sample was observed by transmission electron microscopy (TEM). The sample size of the TiC/Mo alloy was a $\phi 3$ mm*2 mm disc. The TEM foil was prepared by sanding and ion thinning. The working voltage of the TEM instrument was 120 kV (JEM-3200FS). An X Perth Pro multifunctional X-ray diffractometer (XRD) was used to analyse the phase composition of the material. A Cu target was used for testing, the scanning speed was $4^\circ/\text{min}$, and the scanning range 2θ was set to $10-90^\circ$.

3. RESULTS AND DISCUSSION

3.1. Microstructure and morphology of TiC-reinforced Mo-based composites

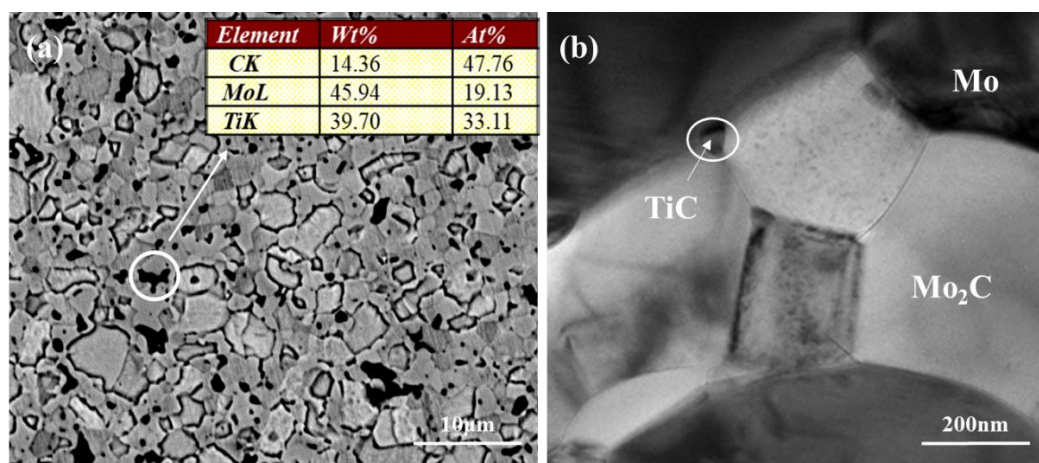


Figure 1. SEM surface morphology and TEM morphology analysis of TiC/Mo alloy: (a) SEM surface morphology and EDS analysis; (b) TEM morphology analysis

Fig. 1 shows the SEM and TEM morphology analysis diagram of the TiC/Mo alloy after sintering. It can be seen that the TiC particles are mainly distributed on the grain boundary and the intersection of the grain boundaries; a small part is distributed inside the crystal, and the TiC particles are distributed inside the crystal grain, which are smaller. According to the literature [21], the presence of second-phase particles can refine the molybdenum grains because the second-phase particles on the grain boundaries can play a pinning role and hinder the growth of the grains. According to the energy spectrum analysis in Fig. 1(a), TiC particles contain a certain amount of the Mo element, which is caused by a solid solution of Mo infiltrating into TiC particles during high-temperature sintering. TiC is more likely to react with oxygen than molybdenum at high temperatures, generating TiO_2 and remaining in the matrix [22].

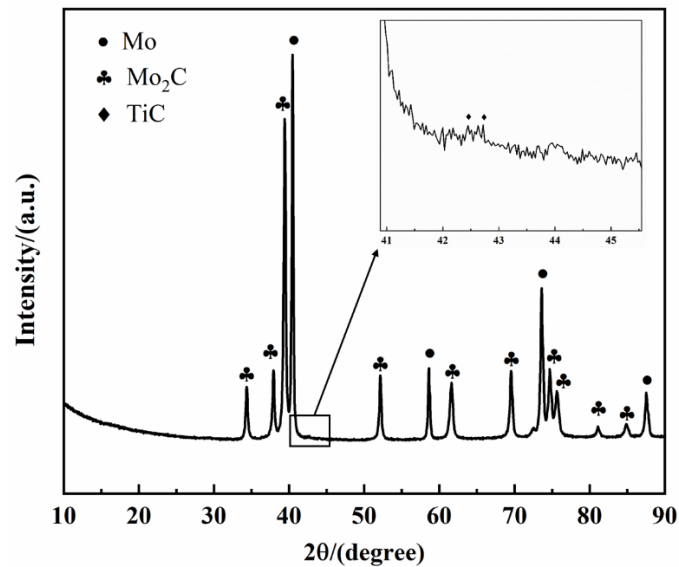


Figure 2. XRD phase analysis of the TiC/Mo composite

Fig. 2 shows the XRD image of the TiC/Mo composite prepared after sintering. It can be seen in this figure that the sintered sample is mainly composed of Mo and Mo₂C. The amount of TiC added is small, and the presence of its peak is not significant. It can also be seen in Fig. 2 that there is a large amount of Mo₂C phase because a graphite mould was used in the sintering process. During the high-temperature sintering process, the carbon in the mould enters the powder and reacts quickly with the molybdenum metal, producing a large amount of molybdenum carbide.

3.2. Potentiodynamic polarization curve analysis

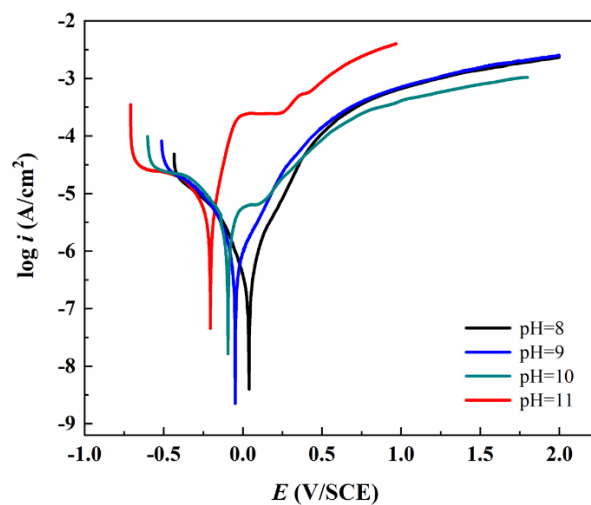


Figure 3. Potentiodynamic polarization curves of TiC/Mo composites at different pH values

Fig. 3 shows the polarization curve obtained by electrochemical corrosion of the TiC/Mo alloy at different pH values. From the overall analysis of the polarization curve, it can be seen that the

corrosion rate of the alloy still exhibits large differences under the four pH values. As the pH value increases, the corrosion potential of the alloy continues to decrease, and the corrosion current continues to increase. When the pH value is low, the dimensional passivation area is not produced in the potentiodynamic polarization curve. As the pH value continues to increase, the dimensional passivation area of the curve becomes more prominent, and the dimensional passivation current area also continues to widen. When the potentiodynamic polarization curves of the TiC/Mo composite materials in the pH 10 and 11 solutions showed an obvious dimensional passivation area, a passive film was formed on the surface and horizontal area of the composite material.

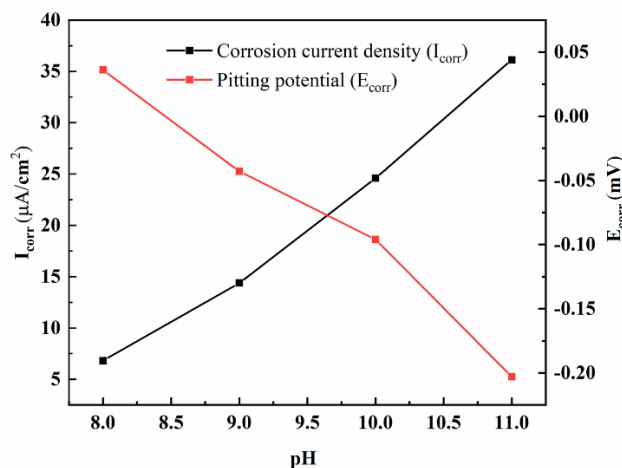


Figure 4. Corrosion current density and corrosion potential of TiC/Mo composites under different pH values

Fig. 4 shows a trend graph of the corrosion current density and corrosion potential of TiC/Mo composites under differing pH environments. It can be seen in Fig. 4 that the corrosion current density of the TiC/Mo composite electrode reaction shows a gradual increase with a corresponding gradual increase in the pH value. The corrosion resistance is best when the pH is 8. It can also be seen in Fig. 4 that as the pH value continues to increase, the corrosion potential shows a continuous downward trend, and the TiC/Mo composite exhibits the best corrosion resistance performance at pH=8. When the TiC/Mo composite material undergoes electrochemical corrosion under alkaline conditions, it becomes easier to accumulate a large amount of OH^- in impurity-rich areas, irregular surfaces and narrow gaps. Metal dissolution and cathodic reduction reactions occur on the surface of the etched hole. As the reaction progresses, the oxygen in the pits gradually becomes consumed, and oxygen depletion occurs. While the oxidation-reduction reaction is inhibited, the metal continues to dissolve, so the positive charge of the metal in the etching solution is significantly enriched. To maintain the conservation of the charge, more anions in the etching solution are required to migrate into the pores. As the corrosion in the etch hole intensifies, the oxidation-reduction reaction rate of the adjacent surface also increases, so the surface of the outer area of the etch hole is cathodically protected, and the corrosion is limited.

The annual corrosion depth in different pH solutions is calculated according to the conversion formula of annual corrosion current and annual corrosion depth [23]. As a result, the annual corrosion depth of the TiC/Mo composite prepared by spark plasma sintering increases with the corresponding

increase in pH. The maximum corrosion depth is 6.093×10^{-2} mm/year in a pH=11 solution, and the minimum corrosion depth is 1.150×10^{-2} mm/year in a pH=8 solution. When the pH= 9 and 10, the annual corrosion depth is 1.413×10^{-2} mm/year and 4.149×10^{-2} mm/year, respectively. It can be seen that when the pH is increased to 10, the corrosion effect of OH⁻ ions on the composite material is significantly improved, which also matches the result of the polarization curve in Fig. 3.

3.3. Electrochemical impedance spectroscopy (EIS) analysis

Fig. 5 shows the AC impedance spectra of TiC/Mo composites under differing OH⁻ concentrations. Fig. 5(a) shows a Nyquist diagram of the composite material under different OH⁻ concentrations. Fig. 5(a) shows that the TiC/Mo composite exhibits a single capacitive arc characteristic under three different OH⁻ concentrations. In addition, with decreasing OH⁻ concentration, the arc radius of the TiC/Mo composite gradually decreases, indicating that its corrosion resistance decreases as the OH⁻ concentration decreases.

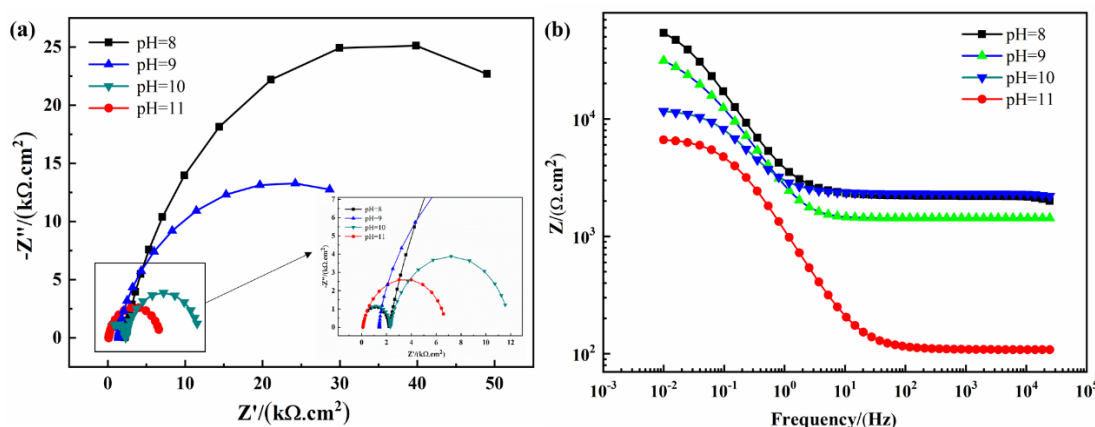


Figure 5. AC impedance spectroscopy of TiC/Mo alloy at different pH values

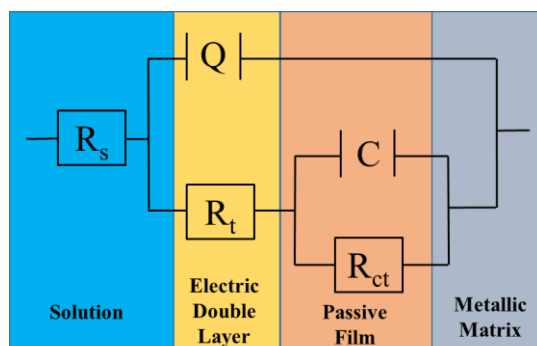


Figure 6. Equivalent circuit diagram for fitting AC impedance spectrum data of TiC/Mo alloy.

Fig. 5(b) shows the Bode diagram of TiC/Mo composites at differing OH⁻ concentrations. It can be seen in Fig. 5(b) that as the pH value continues to increase, the resistance film value continues to

decrease, and the corrosion resistance gradually weakens. It can also be seen that as the corrosion of the material progresses, its phase angle tends to 0, which provides an indication that there are corrosion products on the surface of the TiC/Mo composite [24].

Using the equivalent circuit corresponding to the AC impedance spectra of the TiC/Mo composite material at different pH values, as shown in Fig. 6, ZSimpWin software was used to fit the AC impedance spectra of the TiC/Mo composite material at four different pH values. The best-fitting equivalent circuit is an R(Q(R(QR))) -type circuit. R_s is the solution resistance. Q_{dl} and C are the constant phase angle components of the electric double-layer capacitor formed between the etching solution and the working electrode surface. R_t is the film resistance. R_{ct} is the charge transfer resistance.

Fitting the equivalent circuit R(Q(R(QR))) shown in Fig. 6 to the AC impedance spectra of TiC/Mo composites in different OH⁻ concentration etching solutions, the results can be obtained as shown in Table 1. The parameters of each circuit component are shown. From the data in Table 1, it can be seen that the charge transfer resistance R_{ct} decreases continuously as the pH value increases. Among them, the pH dropped significantly from the R_{ct} value of 9. The R_{ct} resistance at pH=8 is reduced by two orders of magnitude compared to pH=11, providing an indication that the corrosion solution greatly promotes the flow of ions on both sides of the passivation film, strengthens the interaction and promotes the accumulation of a large amount of OH⁻ on the surface of the passivation film. Ions easily reach the critical concentration that causes the rupture of the passivation film. In addition, the transmission resistance of ions and charges is reduced during the corrosion process, which leads to an acceleration of the destruction process of the alloy passivation film and improves the corrosion rate of the alloy. This conclusion is consistent with the measurement result of the polarization curve in Fig. 3..

Table 1. Fitting data of AC impedance spectra of TiC/Mo composites under different pH conditions

pH	R_s ($\Omega \cdot \text{cm}^2$)	Q_{dl} ($\text{F} \cdot \text{cm}^{-2}$)	R_t ($\Omega \cdot \text{cm}^2$)	C ($\text{F} \cdot \text{cm}^{-2}$)	n	R_{ct} ($\Omega \cdot \text{cm}^2$)
8	6.26×10^{-6}	1.34×10^{-9}	2.21×10^3	8.57×10^{-5}	0.80	6.68×10^4
9	1.43×10^{-3}	6.65×10^{-5}	2.37×10^3	6.66×10^{-5}	0.52	4.70×10^4
10	1.00×10^{-2}	9.10×10^{-10}	2.31×10^3	1.56×10^{-4}	0.86	9.70×10^3
11	1.08×10^2	1.80×10^{-4}	6.39×10^3	4.97×10^{-3}	1.00	3.38×10^2

3.4. Corrosion surface morphology analysis

Fig. 7 shows a picture of the surface morphology of TiC/Mo composites after corrosion in solutions with different pH values. It can be seen in Fig. 7 that the electrochemical corrosion of the TiC/Mo composites in solutions with different pH values all show the characteristics of pitting corrosion. The pitting corrosion on the surface of the TiC/Mo composite material is obvious, and the pore depth and corrosion strength both deepen and strengthen with the increase in the pH value of the corrosive solution. When the pH value is low, the effect of pitting corrosion is weak, and erosion occurs in some areas of the alloy, but only dark grey spots appear. These spots serve as the appearance of the initial

corrosion. As the pH value of the solution increases, the corrosion area and depth continue to increase. When the pH value is 11, the corrosion becomes more intense, and the corrosion depth increases significantly. These pitting corrosion areas gradually evolve into uneven surface corrosion morphology and further aggravate the corrosion of the metal surface. They then continue to corrode into the metal in this manner. In addition, under all OH^- concentration conditions, TiC/Mo composites exhibit metastable pitting corrosion, indicating that OH^- is easily transferred to the alloy/oxide interface through the passivation film [25].

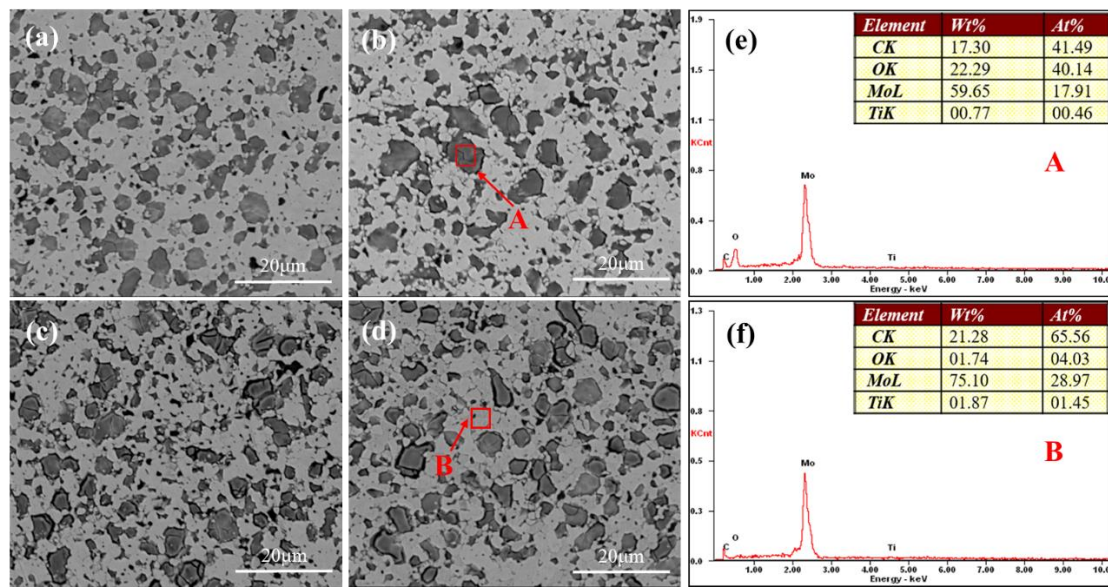


Figure 7. Surface scanning photos and EDS analysis of TiC/Mo composites after corrosion in solutions with different pH values (a) pH=8; (b) pH=9; (c) pH=10; (d) pH=11; (e) -(f) EDS analysis of the composition of spectrum A-B

Fig. 7 (e-f) shows the EDS energy spectrum analysis diagram of the TiC/Mo composite material in solution. Fig. 7(e) shows the energy spectrum analysis, which found that the element content of the material is almost the same as the composition of the sample that was not corroded, indicating that the influence of corrosion in this area is small. Fig. 7(f) shows the energy spectrum analysis of the corroded area, and the result shows that the oxygen content has increased greatly. This is because a large amount of molybdenum oxide is formed on the corroded surface. The TiC/Mo alloy undergoes an oxidation-reduction reaction under the action of an electric current and an oxide in the form of a film, and an agglomerated structure is formed to cover the surface of the alloy matrix. This passivation film is easily destroyed by the dissolution of OH^- radicals from the solution. Therefore, it can be judged that the oxide on the corroded surface is a dense film composed of MoO_2 and $\text{MoO}(\text{OH})_2$ [26].

4. CONCLUSION

This article mainly discusses the preparation of a TiC/Mo alloy by the SPS sintering method. According to an analysis of its structure and mechanical properties, the TiC/Mo alloy meets the

requirements of engineering applications. In addition, at room temperature, the corrosion performance in alkaline solutions with different pH values was also explored. The conclusions are as follows:

(1) Electrochemical tests show that different pH values have a greater impact on the electrochemical corrosion rate of TiC/Mo alloys. The corrosion resistance of the TiC/Mo alloy gradually decreases with increasing pH, indicating that the corrosion tendency of the alloy gradually increases. The TiC/Mo alloy has very obvious passivation characteristics starting from a pH value of 10.

(2) The analysis of SEM images shows that with increasing pH, the severity of surface corrosion of the TiC/Mo alloy gradually increases. Corrosion is caused by pitting at places where alloying elements are added, impurity-rich areas, irregular surfaces and narrow cracks. As the degree of corrosion intensifies, the corrosion pits gradually change from black or dark brown ring-shaped spots to a vortex-like uneven corrosion morphology. The confluence of corrosion vortices further aggravates the corrosion of the alloy surface.

(3) The TiC/Mo alloy undergoes an oxidation-reduction reaction under the action of electric current, leading to oxides in the form of film and agglomerated structure being formed to cover the surface of the alloy matrix. With the extension of the corrosion time, the corrosion continues to deepen into the substrate, and a large number of corrosion holes and grooves appear on the surface of the alloy, which gradually reduces the bonding force between the corrosion layer and the substrate. Finally, the bonding force is completely lost and separated from the substrate and falls off.

ACKNOWLEDGEMENT

Project was supported by Key Laboratory fund general projects (No. 6142905180203).

References

1. I.G. Sharma, S.P. Chakraborty, and A.K. Suri, *J. Alloy. Compd.*, 393 (2005) 122.
2. P. Hu, Y.H. Zhou, and T. Chang, *Mater. Sci. Eng., A*, 687 (2017) 276.
3. H. Sıralı, D. Şimşek, and D. Özyürek, *Met. Mater. Int.*, (2020).
4. W. Zhou, X. Sun, K., Kikuchi, N. Nomura, K. Yoshimi, and A. Kawasaki, *Mater. Des.*, 146 (2018) 116.
5. G. Liu, G.J. Zhang, F. Jiang, X.D., Y.J. Ding, and J. Sun, *Nat. Mater.*, 13 (2013) 344.
6. G.C. Stevens, T. Edmonds, *J. Catal.*, 37(1975)544.
7. K. Bartschat, A. Dasgupta, and J.L. Giuliani, *J. Phys. B-At. Mol. Opt.*, 35(2002)2899.
8. J. F. Stubbins, *J. Nucl. Mater.*, 122(1984)715.
9. J. Peng, P.W. Chung, M. Dubey, and R.R. Namburu, *Nano. Res.*, 11(2018)1541.
10. T. Nagae, S. Kakiuchi, K. Himi, S. Tomida, E. Yamaguchi, and T. Yoneda, *Mater. Sci. Forum.*, 638(2010)2121.
11. G. Chen, J. Liu, X. Shu, B. Zhang, and J. Feng, *Vacuum*, 154(2018)1.
12. M. Tang, A.T. Nelson, E.S. Wood, S.A. Maloy, and Y.B. Jiang, *Scr. Mater.*, 120(2016)49.
13. V.V. Chernov, O.A. Ivanov, V.A. Isaev, D.B. Radishev, and A.V. Kozlov, *Diam. Relat. Mater.*, 37(2013)87.
14. P. Allen, X. Chen, *J. Mater. Process. Tech.*, 186(2007)346.
15. V. P. Martínez, C. Aguilar, J. Marín, S. Ordonez, and F. Castro, *Mater. Lett.*, 61(2007)929.
16. S. Tamilselvi, T. Nishimura, X.H. Min, and K. Tsuzaki, *Mater. T. Jim*, 50(2009)2545.
17. W.C. Moshier, *J. Electrochem. Soc.*, 134(1987)2677.

18. Q. Zhang, N. Lin, and Y. He, *Int. J. Refract. Met. H.*, 38(2013)15.
19. O.A. Abu-Zeid, R.I. Bates, *Surf. Coat. Tech.*, s 86(1996)526.
20. H.H. Uhlig, P. Bond, and H. Feller, *J. Electrochem. Soc.*, 110(1963)650.
21. A.G. Gad-Allah, H.A.A. El-Rahman, and M.M. Abou-Romia, *J. App. Electrochem.*, 18(1988), 86-91.
22. J. Xu, T. T. Sun, S. Jiang, P. Munroe, and Z.H. Xie, *Appl. Surf. Sci.*, 447(2018)500.
23. S. Lan, P. J. Sheng, *J. Mater. Eng.*, 53(2001)31.
24. V. Diaz, E. Teliz, F. Ruiz, P.S. Martinez, R. Faccio, and F. Zinola, *Int. J. Hydrogen Energy*, 38(2013)12811.
25. Z. Yong, J. Zhu, C. Qiu, and Y. Liu, *Appl. Surf. Sci.*, 255(2008)1672.
26. K. Hashimoto, N. Kumagai, H. Yoshioka, J.H. Kim, E. Akiyama, and H. Habazaki, *Corros. Sci.*, 35(1993)363.

© 2020 The Authors. Published by ESG (www.electrochemsci.org). This article is an open access article distributed under the terms and conditions of the Creative Commons Attribution license (<http://creativecommons.org/licenses/by/4.0/>).